Analysis of Dominant Terms in Reynolds-Stress Budgets for a Hot Free Subsonic Jet Using Large-Eddy Simulation

Basile Desmolin, Emmanuel Laroche, Julien Troyes, Adrien Langenais

AIAA Aviation Forum and ASCEND co-located Conference Proceedings
29 July - 2 August 2024, Las Vegas, Nevada
AIAA AVIATION FORUM AND ASCEND 2024

10.2514/6.2024-3869

Analysis of dominant terms in Reynolds-stress budgets for a hot free subsonic jet using Large-Eddy Simulation

B. Desmolin*, E. Laroche†, J. Troyes‡
ONERA/DMPE, Université de Toulouse, F-31055, Toulouse, France

A. Langenais§
ONERA/DMPE, Université Paris Saclay, F-91123, Palaiseau, France

Bridges reference hot subsonic jet is simulated using a Reynolds Stress Model. The obtained results confirm that this approach, even if sophisticated, is not satisfactory and it requires extra-modelling efforts. Then, a LES is set up to compute the Reynolds Stress budgets. The LES is first validated by comparing average fields obtained with that measured by Bridges. Since the differences are small, the terms making up the Reynolds stress balance are computed from processing the archived unsteady quantities. The two main regions studied are the potential area and the self-similar area. The results show a dominance of production and pressure strain correlation terms close to the convergent nozzle exit. In the self-similar area, turbulent diffusion and dissipation become significant, and the convection term becomes non-negligible. On the other hand, pressure and viscous diffusion terms remain negligible far from the walls. These results emphasize the importance of accurately modelling the redistribution term.

Nomenclature

Symbols

x, y, z	=	Cartesian coordinates [m]
r	=	Radial coordinate [m]
θ	=	Orthoradial coordinate
D	=	Convergent nozzle diameter [m]
Δr	=	Mesh spacing [m]
L	=	Characteristic size [m]
u_i	=	Instant velocity component [m.s^{-1}]
p	=	Pressure [Pa]
T	=	Temperature [K]
ρ	=	Density [kg.m^{-3}]
ν	=	Kinematic viscosity [m^2.s^{-1}]
μ	=	Dynamic viscosity [Pa.s]
k	=	Turbulent kinetic energy [m^2.s^{-2}]
S_{ij}	=	Strain tensor [s^{-1}]
τ_{ij}	=	Viscous stress tensor [Pa]
Δ	=	LES cut-off characteristic size [m]
$\mathcal{V}$	=	Volume of a cell [m^3]
$\mathcal{A}$	=	Surface area of a cell [m^2]
a	=	Speed of sound [m.s^{-1}]
$\delta_{0.5}$	=	Half-velocity jet radius [m]
C_S	=	Smagorinsky constant
η	=	Self-similarity parameter
M	=	Mach number

*PhD Student, ONERA (DMPE/HEAT), basile.desmolin@onera.fr
†Research Scientist, ONERA (DMPE/HEAT), emmanuel.laroche@onera.fr
‡Research Scientist, ONERA (DMPE/STAT), julien.troyes@onera.fr
§Research Scientist, ONERA (DMPE/MPF), adrien.langenais@onera.fr

M_a = Acoustic Mach number
δ_{ij} = Kronecker tensor

Subscripts

∞ = Ambiant condition
j = Nozzle exit condition
t = Turbulent variable

Superscripts

$\tilde{}$ = Favre average
$''$ = Favre fluctuation
$-$ = Reynolds average
$'$ = Reynolds fluctuation
r = Subgrid variable

I. Introduction

PROPULSIVE jets are complex flows that can evolve under extreme conditions due to the high speeds and temperatures encountered. The study of hot supersonic jets is motivated by various needs, including the reduction of noise induced by launchers [1] on a launch pad, which places heavy constraints on the rocket, its payload and the surrounding structures. Research is also being carried out in the military field, in which a good understanding of the physics and structure of these jets is essential, particularly for the assessment of infrared signatures [2]. In addition, predicting the ejection temperature is very important when sizing the nozzle. It must be able to resist temperatures over 3000 K [3].

Many experimental studies were performed on subsonic [4–8] and supersonic jets [9–13]. In particular, they made it possible to understand the complex structure of these flows using Schlieren images [9] and hot/cold wires [7]. These studies highlighted the presence of a potential core, defined as an area without mixing between the fluid leaving the jet and the ambient air, whose length depends strongly on the Mach [14] and the Reynolds numbers [15]. Downstream of this zone, there is a so-called self-similar area. Several variables, such as velocity and Reynolds stresses, depend only on a self-similarity parameter η [16]. This area generally starts further upstream for the velocity than for the second-order moments [17]. Finally, the study of the influence on the noise generated by jets of certain parameters such as the Mach number [10], temperature [11] and nozzle pressure ratio [12] led to the creation of several databases.

These studies took advantage of technological advances in measurement techniques such as Laser Doppler Velocimetry (LDV) or Particle Image Velocimetry (PIV) to obtain increasingly complete and accurate data, particularly for measuring Reynolds stresses. However, the limitations of these campaigns are that they are very costly to set up and difficult to apply to complex configurations such as those used in the aerospace industry. As a result, numerical simulation of these flows is playing an increasingly important role in current research. Several unsteady jet simulations [18–24] were also carried out. They resulted in a complete archiving of various turbulent quantities such as the double [22] and triple [24] moments of the velocity, leading to a better understanding of the jet physics.

Some Reynolds-Averaged Navier-Stokes (RANS) simulations of propulsive jets were performed by Dash *et al.* [25–27] and Georgiadis *et al.* [28]. These studies revealed the large discrepancies between the turbulence models. No model correctly predicts the entire jet. This is partly because turbulence models are generally calibrated for boundary layer flows rather than free shear flows [29]. RSM models transporting Reynolds stresses are not immune to this problem. The Reynolds stress transport equation is made up of convection, production, dissipation, diffusion and redistribution terms. Eisfeld [30] showed that the constants used in the Speziale Sarkar Gatski (SSG) model [31] for the redistribution term do not provide the right level of turbulent anisotropy in a mixing layer. The redistribution term dispatches the turbulent kinetic energy between the different Reynolds stresses, and is responsible for restoring isotropy to the turbulence. Experimental studies by Panchapakesan *et al.* [32] and Toutiaei *et al.* [33] as well as numerical simulations proposed by Pantano *et al.* [24], Colombié *et al.* [23] and Bogey *et al.* [22] confirmed that the redistribution term is dominant in shear flows. Correct modelling of this term is therefore essential.

Although most propulsive jets are supersonic, the following study focuses on a heated subsonic jet. Supersonic jets involve a large number of physical phenomena such as compressibility, thermal effects, shocks and expansion beams. It

is therefore appropriate to validate the calculation and post-processing routine on a hot subsonic case before moving to the study of hot supersonic jets.

The following article is divided into five parts. First, the studied jet is defined, and the experimental set up is described. Next, RANS modelling of this jet is performed using the Elliptic Blending Reynolds-Stress Model [34] (EBRSM) transporting Reynolds stresses tensor. The results being not convincing, so a Large-Eddy Simulation (LES) is set up to directly compute the component terms of the Reynolds stress transport equation. As a result, the third part introduces the computational domain, the meshes and the fourth one a comparison of mean fields obtained with LES and experimental data. Finally, the fifth part presents an analysis of the balance terms of the Reynolds stress transport equation in the two main jet regions.

II. Experimental case

A. Experimental set-up

The experimental case is an axisymmetric subsonic air jet experimentally tested by Bridges and Wernet [35]. Their study aimed to provide PIV data on a wide range of turbulent isothermal or anisothermal jets. The jet is generated using a simple convergent nozzle with an exit diameter of $D = 0.0508$ m. The nozzle geometry is represented in Fig. 1.

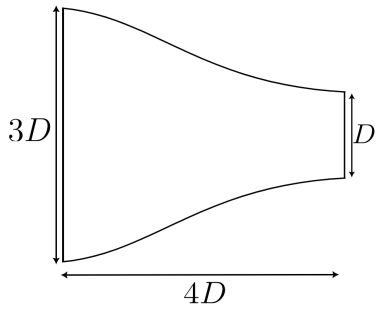

Fig. 1 Convergent dimensions.

The experimental conditions for the whole range of tests performed are described in Table 1, with ambient conditions $p_\infty = 101\,300$ Pa and $T_\infty = 294$ K. The acoustic Mach number and design Mach number are defined respectively in Eq. 1 and 2.

$$\mathrm{M_a} = U_j / a_\infty \tag{1}$$

$$\mathrm{M} = U_j / a_j \tag{2}$$

Table 1 Experimental conditions.

Test number	$\mathrm{M_a}$	M	T_j/T_∞	p_j/p_∞
1	0.500	0.513	0.950	1.197
2	0.900	0.985	0.835	1.861
3	**0.500**	**0.376**	**1.764**	**1.102**
4	0.900	0.678	1.764	1.375
5	1.330	1.001	1.764	1.888
6	0.900	0.548	2.700	1.219
7	1.485	0.904	2.700	1.678

The focus of the study being temperature effects on the shear layer development, a hot jet configuration is examined. For this reason, tests 3, 4 and 6 were considered (see table 1). Case 3 was already retained by NASA [36] as a validation

case for the RANS turbulence models. This case is thus chosen to compare the results of our study with those found in the literature. For this case, the ejection velocity is $U_j = 171$ m.s^{-1} and the temperature is $T_j = 534$ K, with a Reynolds number $\mathrm{Re}_j \approx 78\,000$.

B. Experimental results

Measurements of the velocity field, Reynolds stresses and turbulent kinetic energy, whose expression is defined by Eq. 3, were obtained using a PIV plane for $x \in$ [1D, 25D] and $y \in$ [-1.4D, 1.4D] taking the centre of the convergent exit as the origin.

$$k = \frac{1}{2}\left(\overline{u'_x u'_x} + \overline{u'_r u'_r} + \overline{u'_\theta u'_\theta}\right) \tag{3}$$

These fields, plotted in Fig. 2, indicate the topology of the flow and locate the different areas of the flow represented in Fig. 3. The symmetry of these fields confirms the convergence of the mean flow measurement. Considering the definition of k in Eq. 3 and assessing $\overline{u'_x u'_x} \approx k$ reveals the weak contribution of other stress components and highlights the strong anisotropy of the flow. This is important because most RANS engineering-level turbulence models are isotropic, and therefore satisfy Eq. 4.

$$\overline{u'_x u'_x} \approx \overline{u'_r u'_r} \approx \overline{u'_\theta u'_\theta} \approx \frac{2}{3}k \tag{4}$$

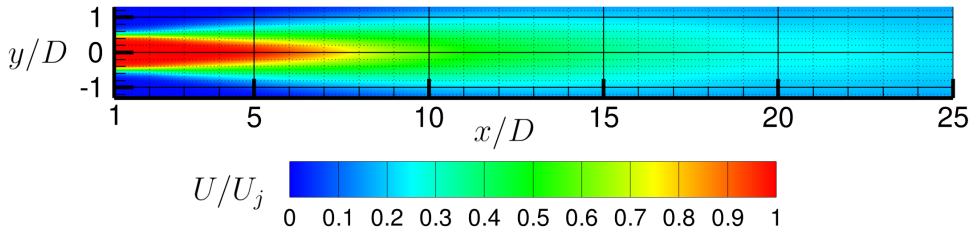

(a) Field of longitudinal velocity scaled by U_j.

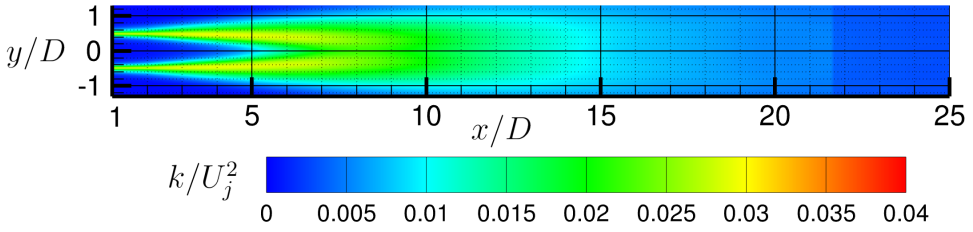

(b) Field of k scaled by U_j^2.

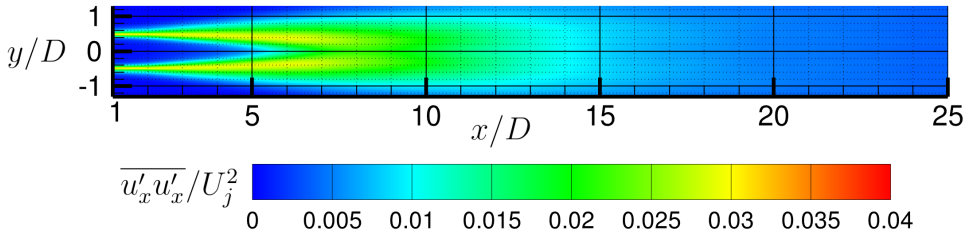

(c) Field of $\overline{u'_x u'_x}$ scaled by U_j^2.

Fig. 2 PIV field measured experimentally by Bridges [35].

To complete these fields, the axial and radial profiles of velocity and turbulent kinetic energy at several axial stations are plotted in Fig. 4 and Fig. 5 respectively. The measurement range is sufficiently large longitudinally to describe the axial evolution of the jet. As a result, the potential core, defined as the area of the jet without mixing with the ambient air, is within the measurement range, as shown in Fig. 4a. From Eq. 5 this core length is 4.8D.

$$U(x = L_c) = 0.99 \times U_j \tag{5}$$

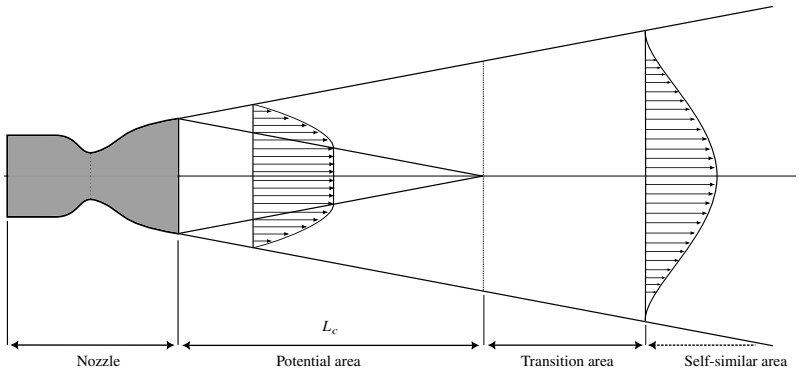

Fig. 3 Schematic drawing of the different areas of a jet.

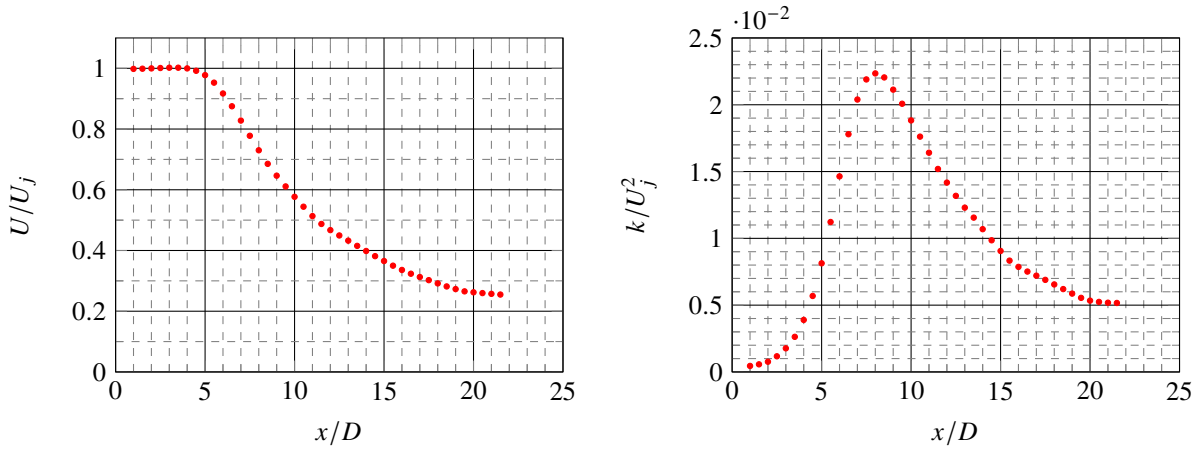

(a) Longitudinal profile of k scaled by U_j^2. **(b) Radial profile of k scaled by U_{axis}^2.**

Fig. 4 Experimental longitudinal profiles of velocity and turbulent kinetic energy along the symmetry line.

However, the measurement area is not radially large enough, so the radial evolution of the various flow quantities is not completely measured for $x > 10$D. This lack of measurement makes the study of the self-similar area more difficult, which defines an area downstream of the potential core where certain quantities such as velocity, temperature and Reynolds stresses depend only on y/x. This area is reached as early as 10D as shown in Fig. 5a for axial velocity, where experimental points at $x = 10$D and $x = 15$D are superimposed, and later for turbulent kinetic energy. It is not possible to obtain the self-similar profile for Reynolds stresses, as the measurement range is too narrow.

III. RANS modelling

A. Computational method

The jet presented in part II is first simulated using RANS modelling. The simulation is performed with the CHARME compressible Navier-Stokes solver of the CEDRE [37] multiphysics code developed by ONERA. This is a cell-centred finite volume code on unstructured meshes. This code has already been used and validated on supersonic jets [38–41], and more generally in the aerospace field [42].

The computation is performed using a 2D axisymmetry model with a 2nd-order Monotonic Upstream-centered Scheme for Conservation Laws (MUSCL) reconstruction for face interpolation using the k-exact method [43]. Flux are calculated using a Harten-Lax-van Leer-Contact [44] (HLLC) scheme. These numerical methods are described in detail

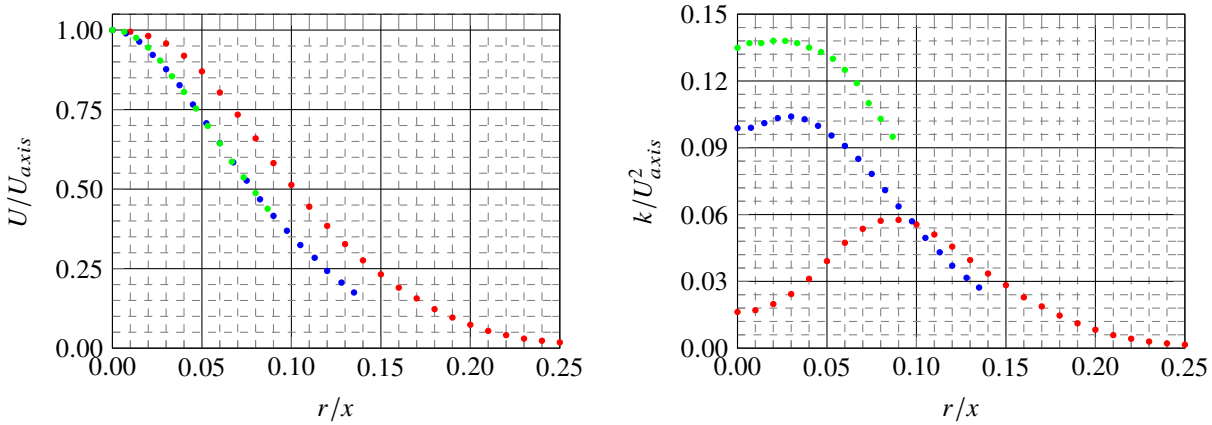

(a) Radial profile of axial velocity scaled by U_{axis}. **(b) Radial profile of k scaled by U^2_{axis}.**

Fig. 5 Experimental radial profiles of velocity and turbulent kinetic energy at several axial stations: • $x = 5D$, • $x = 10D$, • $x = 15D$.

Table 2 Boundary conditions values.

T_{ref}	294 K
p_{ref}	101 300 Pa
M_{ref}	0.01
P_0	111 500 Pa
T_0	534 K

by Courbet *et al.* [45]. The computation is carried out with a 1st-order time implicit scheme, with a local time step set at $CFL_{loc} = 20$ in each cell.

As the flow under study is compressible, Favre notation is used to separate the flow variables into an average part and a fluctuating part as written in Eq. 6, to preserve the classical form of mass conservation [46]. The Favre mean is defined in Eq. 7.

$$u_i = \widetilde{u_i} + u_i'' \tag{6}$$

$$\widetilde{u_i} = \frac{\overline{\rho u_i}}{\overline{\rho}} \tag{7}$$

The RANS model used is the EBRSM model [34], transporting Reynolds stresses $\overline{\rho}\widetilde{u_i'' u_j''}$, dissipation ε and a wall damping factor α. This model was validated on a channel flow case by comparison with a direct numerical simulation (DNS) solution [47], with excellent accuracy.

B. Computation domain and mesh

The computation domain is shown in Fig. 6, and the boundary conditions are defined in table 2. Total pressure and total temperature are set upstream of the convergent. The convergent surface is an adiabatic wall. Turbulence levels are set to match the experimental level at $x = 1D$. An external flow is prescribed at $u_x = 3.41$ m.s^{-1}, *i.e.* M= 0.01 and a static temperature at 294 K. This velocity value is suggested as optimal by the study proposed in Turbulence Modelling Resource [36] to stabilise the calculation, while having a negligible influence on the results.

Mesh convergence was carried out by NASA [36], and the intermediate mesh comprising 72 000 elements is selected as representing the best trade-off between accuracy and computational cost.

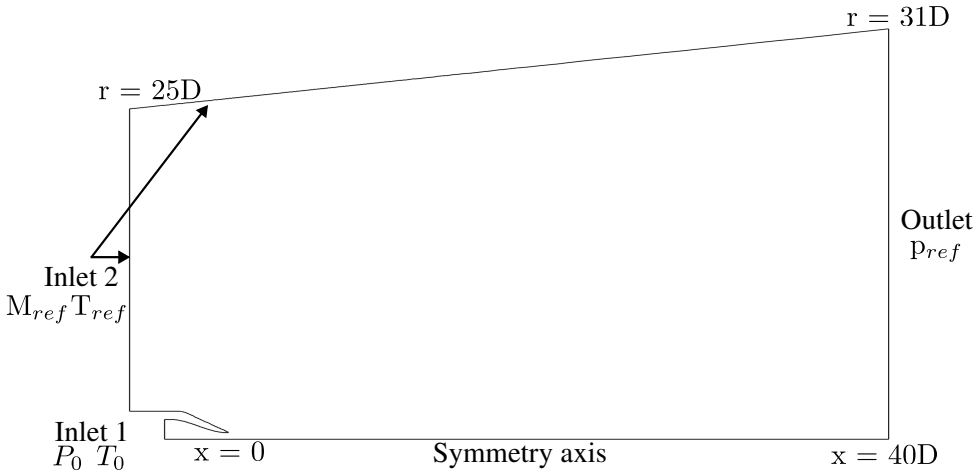

Fig. 6 Computation domain.

C. Results

The axial velocity and Reynolds stress fields are plotted in Fig. 7. Comparison with the PIV fields shown in Fig. 2 highlights that the potential core length is overestimated by the EBRSM model compared with experimental data. Indeed, when looking at Fig. 8a, the model estimates L_c to be $8D$, almost twice as large as that measured experimentally.

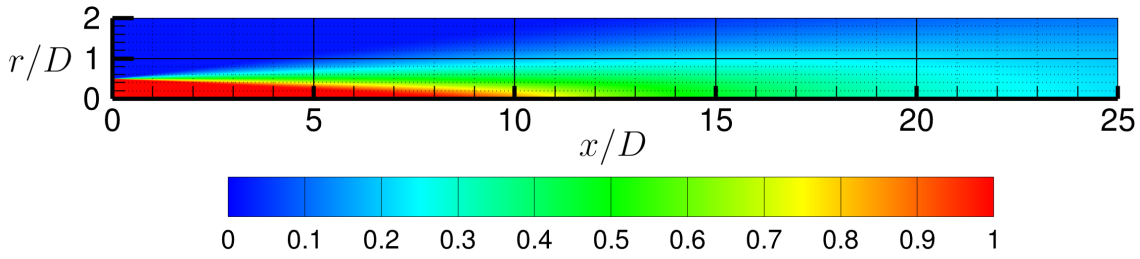

(a) Field of longitudinal velocity scaled by U_j.

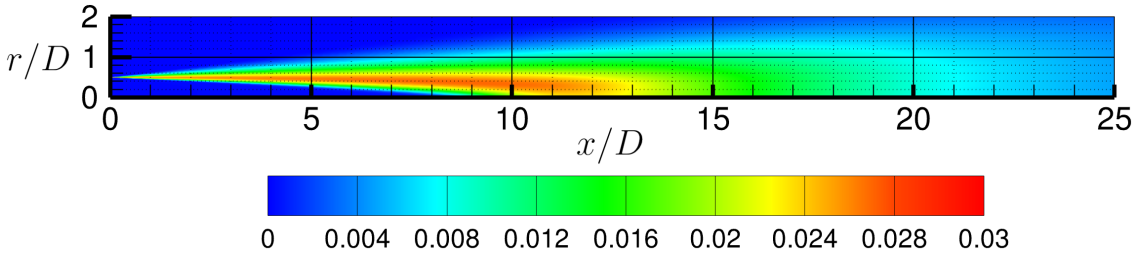

(b) Field of $\widetilde{u_x'' u_x''}$ scaled by U_j^2.

Fig. 7 Axial Reynolds stress and velocity field obtained with the EBRSM model.

Radial velocity profiles plotted at several axial stations in Fig. 8b highlight a significant gap between experimental and simulated data, both in the potential area and in the self-similar area.

The model is therefore poor at predicting propulsive jet behaviour accurately. The potential area is not correctly represented, and the self-similar velocity profile does not match those obtained experimentally. These results are in line with the literature on hot propulsive jet [25–28], which highlights the significant discrepancies between jet RANS simulations and experimental data.

Except for production, each of these terms as to be modelled. However, they are calibrated mostly on homogeneous turbulence or boundary layer cases. A LES is set up to calculate these sub-terms directly on the same case study to

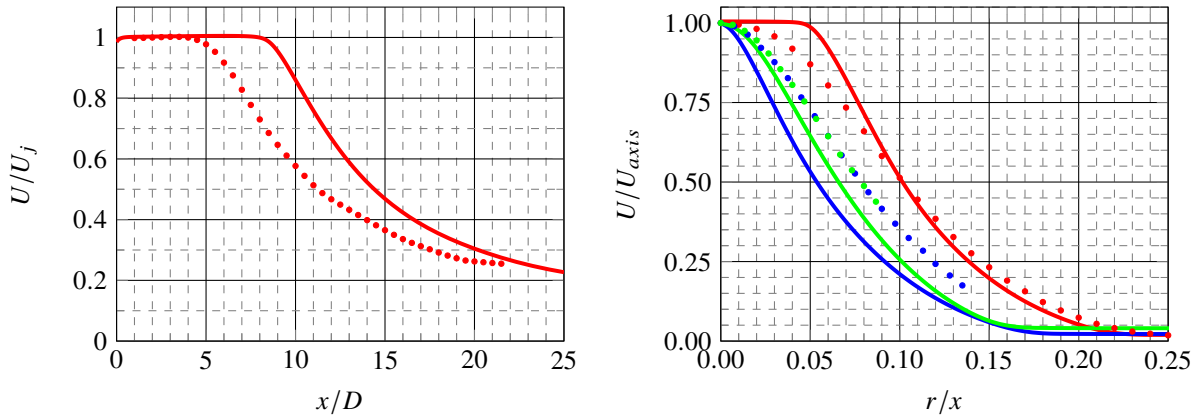

(a) Longitudinal profile of axial velocity along the axis of symmetry: • Exp, — EBRSM.

(b) Radial profile of axial velocity at several axial stations: — $x = 5D$, — $x = 10D$, — $x = 15D$.

Fig. 8 Comparison of EBRSM (—) and experimental (•) velocity profiles.

compare their respective magnitude and influence.

IV. Large-Eddy Simulation

A. Computational method

The quantities are separated into a solved part and a sub-filtered part as indicated in Eq. 8.

$$u_i = \widetilde{u_i} + u_i'' \tag{8}$$

The LES relies on the compressible Navier-Stokes equations described by Vreman *et al.* [48]. The momentum transport equation is detailed in Eq. 9.

$$\frac{\partial \overline{\rho}\widetilde{u_i}}{\partial t} + \frac{\partial \overline{\rho}\widetilde{u_i}\widetilde{u_j}}{\partial x_j} = -\frac{\partial p}{\partial x_i} + \frac{\partial}{\partial x_j}\left(\overline{\tau_{ij}} + \tau_{ij}^r\right) \tag{9}$$

where $\overline{\tau_{ij}}$ is the mean viscous stress tensor and τ_{ij}^r the subgrid stress tensor, defined in Eq. 10 and 11 respectively.

$$\overline{\tau_{ij}} = 2\overline{\mu S_{ij}} - \frac{2}{3}\overline{\mu S_{kk}}\delta_{ij} \tag{10}$$

$$\tau_{ij}^r = \overline{\rho}\left(\widetilde{u_i u_j} - \widetilde{u_i}\widetilde{u_j}\right) \tag{11}$$

The subgrid-scale turbulence model used is the one proposed by Smagorinsky [49] and is detailed in Eq. 12 and 13.

$$\tau_{ij}^r = 2\overline{\rho}\nu_t\left(\widetilde{S_{ij}} - \frac{1}{3}\delta_{ij}\widetilde{S_{ll}}\right) \tag{12}$$

$$\nu_t = (C_S\Delta)\sqrt{2\widetilde{S_{ij}}\widetilde{S_{ij}}} \tag{13}$$

$$\Delta = 2 \times 3 \times \frac{\mathcal{V}}{\mathcal{A}} \tag{14}$$

where C_S is the model constant set to 0.1 and Δ is a LES characteristic cell size, defined Eq. 14.

Computations are 3D with a 2nd-order MUSCL reconstruction for face interpolation using the k-exact method [43] previously mentioned. Flows are calculated using a HLLC [44] scheme. Unlike the RANS calculation, LES is performed through a 2nd-order time integration technique.

B. Computation domain and boundary conditions

The computation domain is an extrusion of the one used for 2D RANS as shown in Fig. 9, with $x \in [-6D, 40D]$, $r \in [0, 25D]$ at $x = -6D$ and $r \in [0, 30D]$ at $x = 40D$. The same boundary conditions are imposed as for the RANS computation.

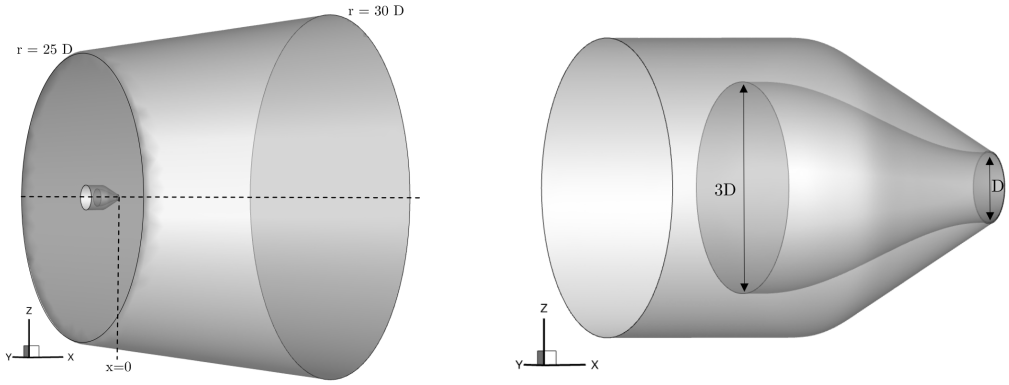

(a) Full calculation domain. **(b) Zoom on the convergent.**

Fig. 9 Representation of the computation domain.

C. Meshes

Two unstructured meshes using tetrahedrons and prisms were created using Centaur software. The main characteristics of these two meshes are described in table 3.

Table 3 Characteristics of the two meshes.

	Number of elements	$\Delta r_{max}/D$	$\Delta r_{min}/D$	$\Delta r/D$ average on the self-similar area ($x = 15D$)	Azimuthal resolution at the nozzle exit
Mesh A	180 millions	0.52	1.8×10^{-4}	0.13	310
Mesh B	210 millions	1.2	1.3×10^{-4}	2×10^{-2}	2000

Two-dimensional cross-sections of the mesh spacing Δr of the two meshes are plotted in Fig. 10a in the whole domain and in Fig. 10b near the nozzle. These fields highlight the three main differences between the two meshes:

1) The longitudinal cell size increases along the symmetry axis, and is smoother and more gradual for mesh B than for mesh A. This is confirmed by the Fig. 11a representing this evolution.
2) A higher azimuthal resolution at the nozzle lip is imposed for mesh B to better capture the mixing layer's early development.
3) The refined zone, designed to capture physical phenomena in the mixing layer, is enlarged for mesh B as shown in Fig. 11b and 11c with the aim of better simulating the evolution of the various turbulent quantities in this part of the flow. A larger mesh size is also imposed further from the jet axis for mesh B, to dissipate potential recirculation areas.

D. Validation of the Large-Eddy Simulation

In order to reduce computational costs, the initial state is interpolated from RANS results with the $k - \omega$ SST [50] turbulence model obtained on a coarser grid. A physical time of 200 D/U_j is computed with the LES on both meshes to evacuate the transient regime. The calculation is carried out on 3120 CPUs for mesh A and 3800 for mesh B. Details of the calculations are summarised in table 4. The RANS calculation used to obtain the initial state has a much lower computational cost with 2600 CPUs during 2 hours.

Converging the average solution of the LES simulation is very costly in terms of computing time, especially for

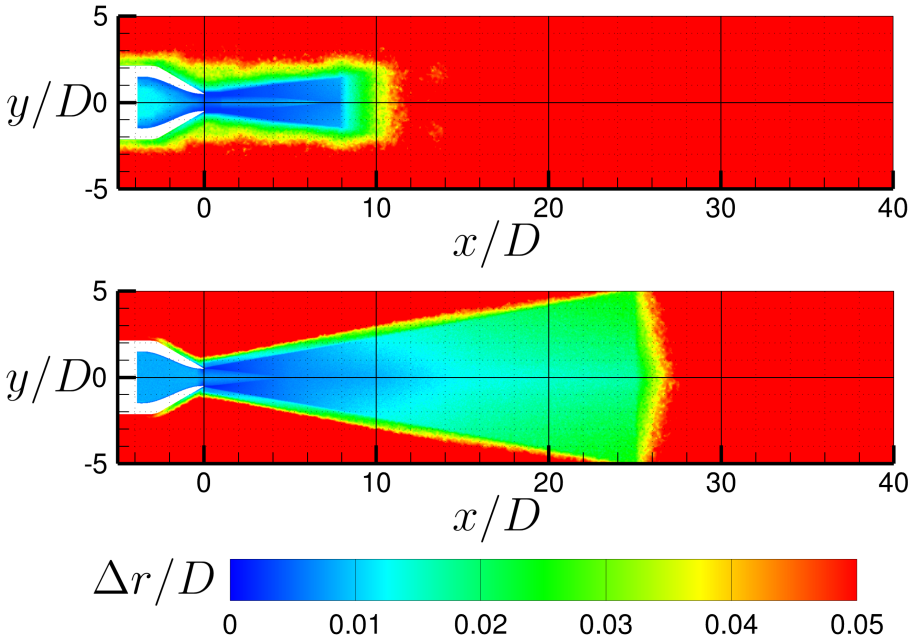

(a) Mesh spacing scaled by D in the jet development region for meshes A (top) and B (bottom).

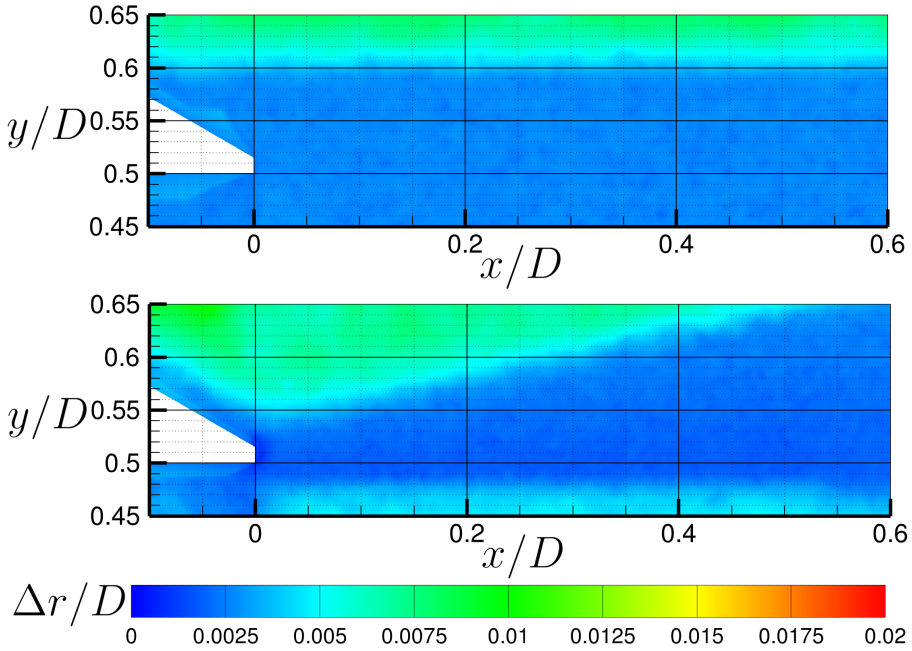

(b) Mesh spacing scaled by D near the base for meshes A (top) and B (bottom).

Fig. 10 2D cross-section of the mesh spacing scaled by D.

third-order moments and gradients. Since the computational domain is axisymmetric, it is possible to perform azimuthal averaging to improve statistical convergence. The Python Antares library [51] is used for this purpose. All the quantities, initially in cartesian coordinates, were converted to cylindrical coordinates, and the computation domain is divided into 1000 slices starting from the x axis. The 1000 slices were averaged, then a $2D$ field is obtained.

As an example, the 2D velocity field obtained after the post-processing on mesh B is shown in Fig. 12.

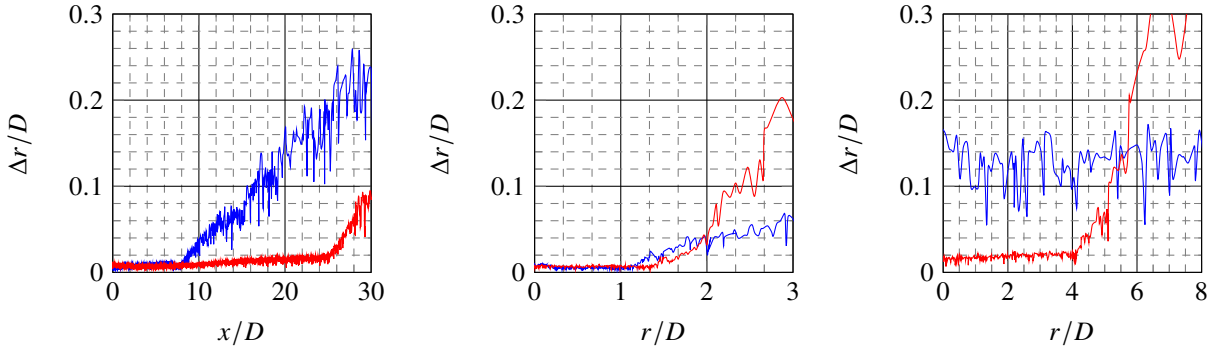

(a) Longitudinal profile at $r = 0$. **(b) Radial profile at $x = 5D$.** **(c) Radial profile at $x = 20D$.**

Fig. 11 Comparison of mesh spacing scaled by D for mesh A (—) and mesh B (—) in different flow zones.

Table 4 Characteristics of the calculations.

	Mesh A	Mesh B
Time step [s]	10^{-6}	5×10^{-7}
Simulated physical time [D/U_j]	700	1000
Number of runs	25	60
Machine time [h.CPU]	990 000	2 400 000
Storage space [To]	3.6	18

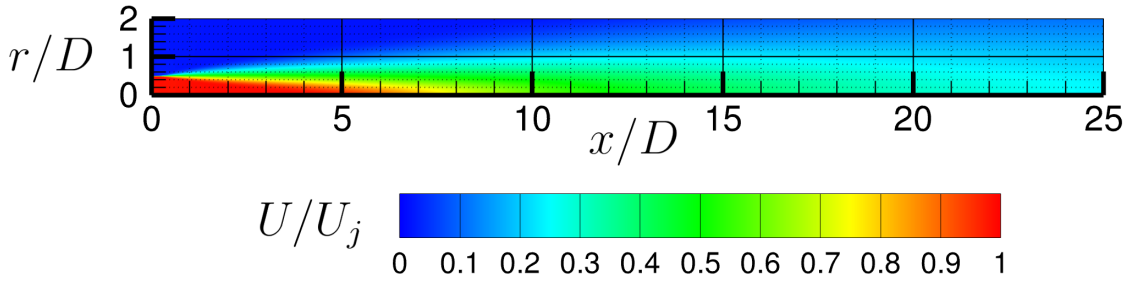

Fig. 12 Average axial velocity 2D fields scaled by U_j using mesh B.

1. Mesh study

Axial velocity and turbulent quantities are plotted in Fig. 13 and 14 for the two meshes and compared with experimental data from Bridges [35].

The longitudinal velocity decay plotted in Fig. 13a is more accurate for mesh B than for mesh A, particularly up to $x = 10D$. The size of the potential core is well reproduced with both meshes. Two slope breaks are present on the longitudinal evolution of turbulent kinetic energy plotted in Fig. 13b with mesh A at $x = 8D$ and $x = 12D$. Mesh B provides an improved distribution, approaching the experimental peak values reached at $x = 8D$.

Longitudinal profiles of velocity and shear rate are plotted in Fig. 13c and 13d respectively, at $y = D/2$. Mesh B has less effect on the results. Overall, axial velocity is well simulated by the two meshes, with an overestimation lower than 5%. However, the shear rate is very different from experimental data. A peak located at $x = 1D$ overestimates this rate by around 100%, but the evolution is well recovered from $x = 10D$. This peak is probably due to a too harsh boundary layer transition leaving the convergent [52, 53]. As the goal is the aerodynamic study of the jet and not the near-wall flow neither aeroacoustics, this is not considered of first order here.

At last, the radial profiles of velocity and shear rate are plotted in Fig. 14a and 14b respectively at $x = 12D$, *i.e.* in the self-similar zone. The velocity profiles obtained with the two meshes are similar to the experimental one. The shear rate is underestimated by 20% with mesh B. However, the evolution is correct. Mesh A gives a value for the maximum

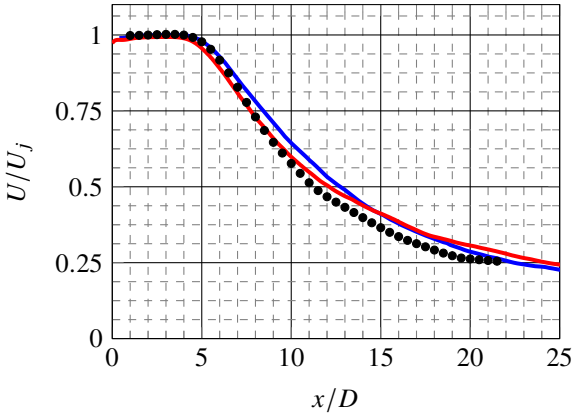

(a) Longitudinal profile of axial velocity along the axis of symmetry.

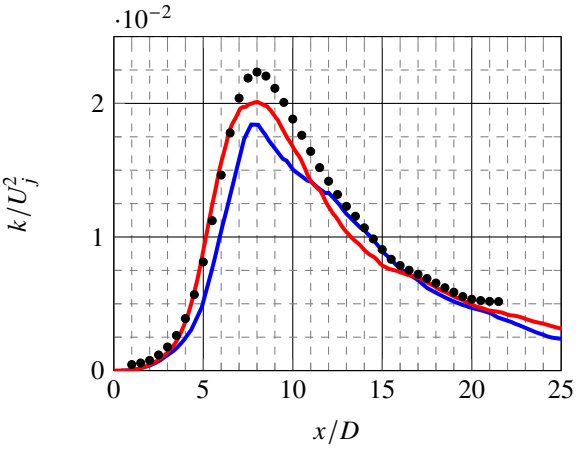

(b) Longitudinal profile of turbulent kinetic energy along the axis of symmetry.

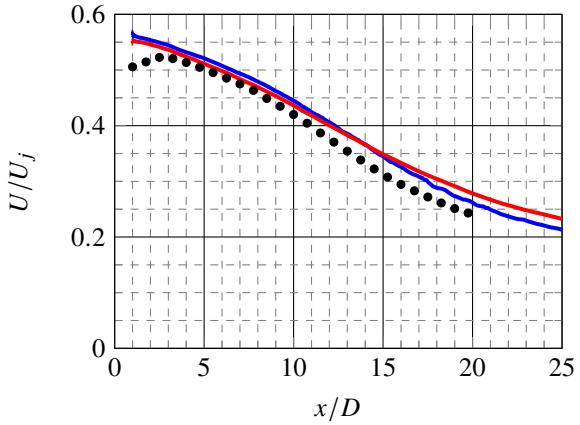

(c) Longitudinal profile of axial velocity in $r = D/2$.

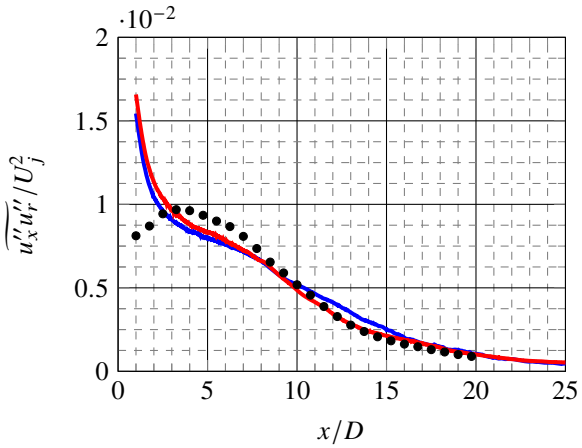

(d) Longitudinal profile of $\widetilde{u_x'' u_r''}$ in $r = D/2$.

Fig. 13 Comparison of longitudinal profiles for mesh A (—), mesh B (—) and experimental data (•).

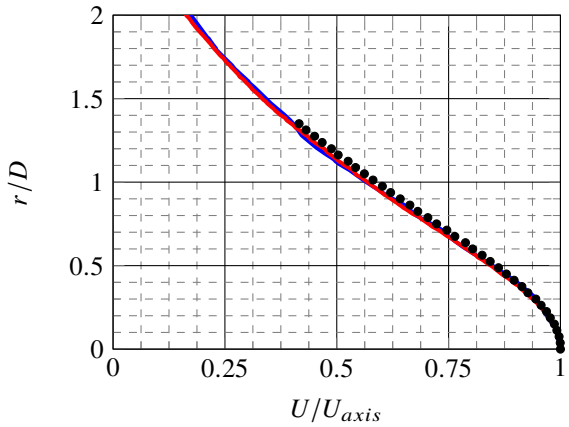

(a) Radial profile of axial velocity at $x = 12D$.

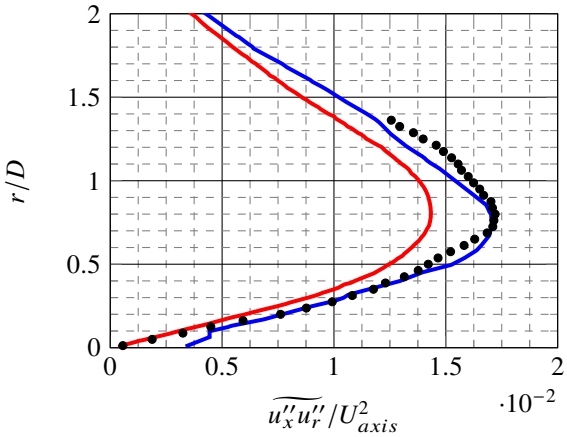

(b) Radial profile of $\widetilde{u_x'' u_r''}$ at $x = 12D$.

Fig. 14 Comparison of radial flow magnitude profiles for mesh A (—), mesh B (—) and experimental data (•).

closer to measured experimentally but is unphysical qualitatively because the shear rate is not zero at the axis, indicating that the flow is not perfectly symmetrical. In addition, spurious slope breaks are visible at $r = 0.1D$ and $r = 1.3D$.

In conclusion, mesh B provides a better simulation of the flow, and is therefore chosen as the reference mesh for the rest of this study.

2. Longitudinal evolution of anisotropy

The longitudinal profile at $r = D/2$ of anisotropy tensor components, defined by the Eq. 15, is plotted in Fig. 15.

$$b_{ij} = \frac{\widetilde{u_i'' u_j''}}{2k} - \frac{1}{3}\delta_{ij} \tag{15}$$

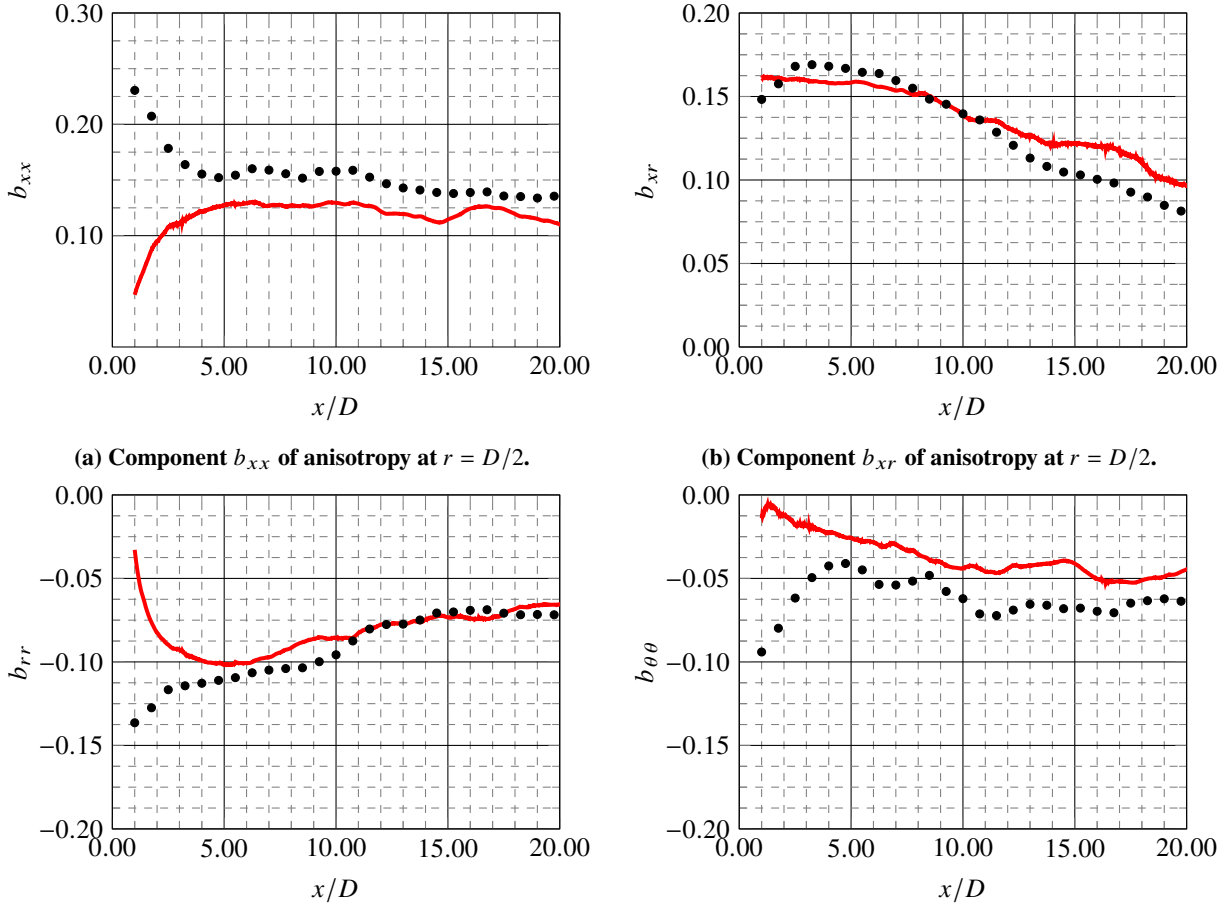

(a) Component b_{xx} of anisotropy at $r = D/2$.

(b) Component b_{xr} of anisotropy at $r = D/2$.

(c) Component b_{rr} of anisotropy at $r = D/2$.

(d) Component $b_{\theta\theta}$ of anisotropy at $r = D/2$.

Fig. 15 Longitudinal profiles of anisotropy components at $r = D/2$ measured experimentally (•) and compute with mesh B (—).

The main information given by these graphs is that the xx, rr and $\theta\theta$ components are non-zero. Turbulence is therefore not isotropic in this region of the jet. The anisotropy components are generally well reproduced, except near the nozzle (*i.e.* $x < 3D$) where the peak in turbulent kinetic energy corresponds to an anisotropy relaxing to zero. The asymptotic values of the xx, rr and $\theta\theta$ components are approximately $b_{xx,\infty} = 0.12$, $b_{rr,\infty} = -0.07$ and $b_{\theta\theta,\infty} = -0.05$ in the self-similar area. The b_{xr} component does not appear to reach a plateau.

The anisotropy values in the self-similar jet area are particularly important because they are used to calibrate the SSG model constants [31]. However, the values of anisotropy measured in a mixed layer and in a boundary layer are very different. As a result, Eisfeld [30] used the anisotropy values obtained in a flat subsonic mixing layer [54] to calibrate this model, which significantly improved the accuracy of the results by obtaining the correct open rate.

3. Radial evolution

Radial profiles of velocity and turbulent quantities are plotted in the potential area and compared with experimental data in Fig. 16.

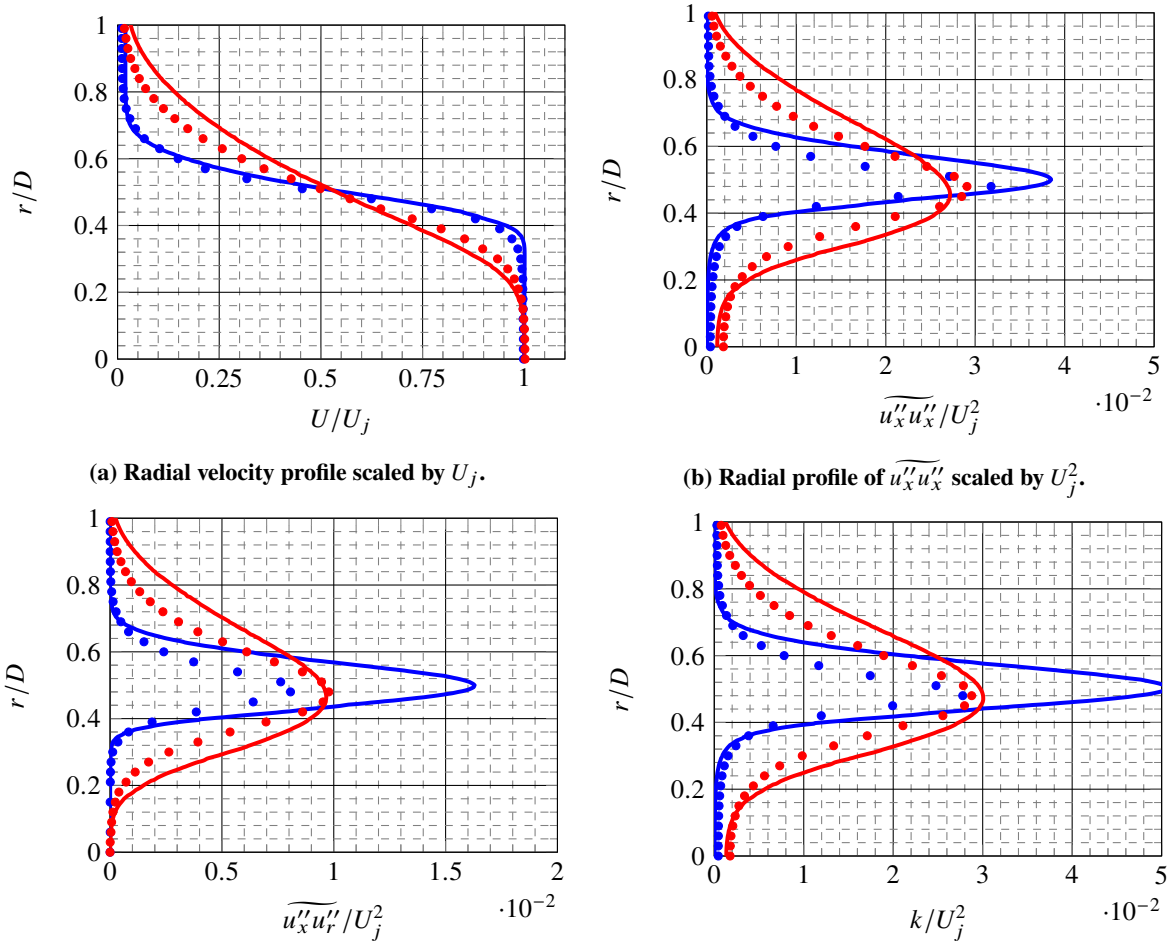

(a) Radial velocity profile scaled by U_j.

(b) Radial profile of $\widetilde{u''_x u''_x}$ scaled by U_j^2.

(c) Radial profile of $\widetilde{u''_x u''_r}$ scaled by U_j^2.

(d) Radial profile of k scaled by U_j^2.

Fig. 16 Radial profiles of velocity and turbulent variables in the potential area measured experimentally (•) and compute with mesh B (—) at several axial stations: — $x = 1D$, — $x = 3D$.

The axial velocity simulated is similar to that measured experimentally. Turbulent kinetic energy is greatly overestimated at $x = 1D$, but this peak is quickly dissipated and a rate similar to the one that was measured experimentally is obtained from $x = 3D$. These profiles validate the correct development of the simulated jet. In particular, the mixing layer spreads correctly close to the nozzle. This is a crucial region, as it largely determines the subsequent structure of the jet.

The same profiles are plotted in the self-similar area of the jet (from $x = 10D$) in Fig. 17. Profiles are not plotted at $x = 15D$ due to the small range of experimental measurements.

The self-similar velocity profile is perfectly reproduced by LES. Turbulence intensity levels are slightly underestimated, notably because the velocity at the U_{axis} is overestimated, but the overall trend is correctly simulated.

The mean field is rendered correctly, both in the potential area and in the self-similar area. As a result, an in-depth study of the Reynolds stress transport equations is possible.

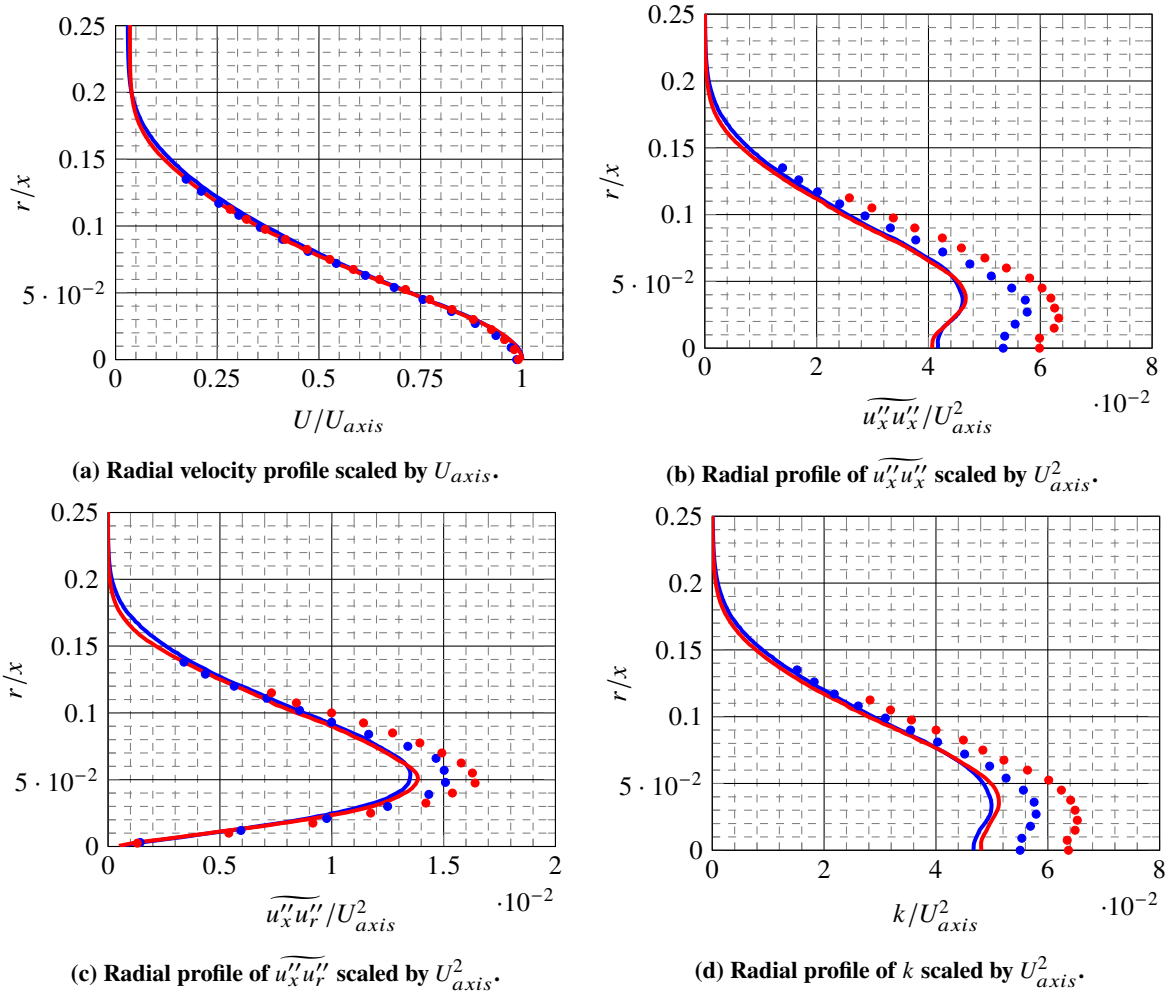

(a) Radial velocity profile scaled by U_{axis}.

(b) Radial profile of $\widetilde{u''_x u''_x}$ scaled by U^2_{axis}.

(c) Radial profile of $\widetilde{u''_x u''_r}$ scaled by U^2_{axis}.

(d) Radial profile of k scaled by U^2_{axis}.

Fig. 17 Radial profiles of velocity and turbulent variables in the self-similar area measured experimentally (•) and compute with mesh B (—) at several axial stations: — $x = 10D$, — $x = 12D$.

V. Reynolds-stress budgets

A. Transport equations

With the results obtained being in close agreement with Bridges data, it is now possible to study the different terms making up the Reynolds stress transport equation. For a compressible flow, this equation reads:

$$\frac{\partial\left(\overline{\rho}\widetilde{u''_i u''_j}\right)}{\partial t} + C_{ij} = \mathcal{P}_{ij} + \phi_{ij} + \mathcal{D}^t_{ij} + \mathcal{D}^p_{ij} + \mathcal{D}^\nu_{ij} - \varepsilon_{ij} + \Sigma_{ij} \tag{16}$$

with the convective term detailed in Eq. 17, as well as the production term 18, the redistribution term 19, turbulent 20, pressure 21 and viscous 22 diffusion terms, dissipation term 23 and mass flow coupling term 24.

$$C_{ij} = \frac{\partial \left(\overline{\rho} \widetilde{u_i'' u_j'' u_k''} \right)}{\partial x_k} \tag{17}$$

$$\mathcal{P}_{ij} = -\overline{\rho} \left(\widetilde{u_i'' u_k''} \frac{\partial \widetilde{u_j}}{\partial x_k} + \widetilde{u_j'' u_k''} \frac{\partial \widetilde{u_i}}{\partial x_k} \right) \tag{18}$$

$$\phi_{ij} = \overline{p' \left(\frac{\partial u_i''}{\partial x_j} + \frac{\partial u_j''}{\partial x_i} \right)} \tag{19}$$

$$\mathcal{D}_{ij}^{t} = \frac{\partial}{\partial x_k} \left(\overline{\rho} \widetilde{u_i'' u_j'' u_k''} \right) \tag{20}$$

$$\mathcal{D}_{ij}^{p} = \frac{\partial}{\partial x_k} \left(\overline{p' u_j''} \delta_{ik} + \overline{p' u_i''} \delta_{jk} \right) \tag{21}$$

$$\mathcal{D}_{ij}^{\nu} = \frac{\partial}{\partial x_k} \left(\left(\overline{\tau_{ik}' u_j''} + \overline{\tau_{jk}' u_i''} \right) \right) \tag{22}$$

$$\varepsilon_{ij} = \left(\overline{\tau_{ik}' \frac{\partial u_j''}{\partial x_k}} + \overline{\tau_{jk}' \frac{\partial u_i''}{\partial x_k}} \right) \tag{23}$$

$$\Sigma_{ij} = \overline{u_i''} \left(\frac{\partial \overline{\tau}_{jk}}{\partial x_k} - \frac{\partial \overline{p}}{\partial x_j} \right) + \overline{u_j''} \left(\frac{\partial \overline{\tau}_{ik}}{\partial x_k} - \frac{\partial \overline{p}}{\partial x_i} \right) \tag{24}$$

Starting again from the equations, it is possible to show that the turbulence in a simple sheared flow is self-sustaining. The mechanism is illustrated in Fig. 18. Shear creates a transverse velocity gradient that produces axial Reynolds stress, which is redistributed to the other components and then partly dissipated. The radial and orthoradial components produce shear stress, which in turn creates $\widetilde{u_x'' u_x''}$, thus forming a cycle.

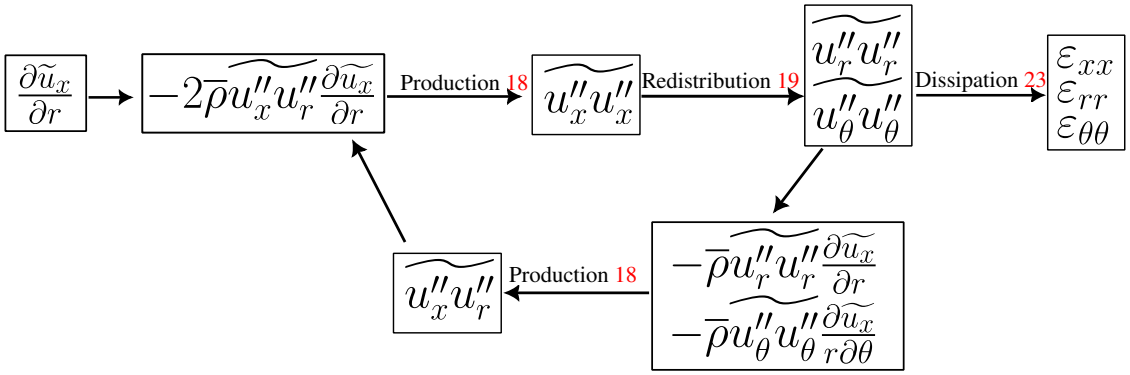

Fig. 18 Turbulence cycle for shear flow, adapted from Leschziner [55].

The LES conducted in this study will verify whether this cycle is occurring. In order to calculate these terms, numerous quantities were archived, including velocity, pressure and temperature, as well as the double and triple products of velocity $\overline{u_i u_j}$ and $\overline{u_i u_j u_k}$, the velocity/pressure correlation $\overline{p u_i}$ and the viscous stress tensor $\overline{\tau}$. Using these stored quantities, it is then possible to compute all the terms making up the Reynolds stress transport equation with the help of relationships 25, 26 and 27.

$$\widetilde{a'' b''} = \widetilde{ab} - \widetilde{a}\widetilde{b} \tag{25}$$

$$\overline{a' b''} = \overline{a' b'} \tag{26}$$

$$\overline{\rho u_i'' u_j''} = \overline{\rho u_i u_j} - \overline{\rho} \widetilde{u_i} \widetilde{u_j} \tag{27}$$

Velocity, pressure and stress tensor gradients were computed directly while other gradients or divergences were computed in post-processing using the Antares python library [51].

Due to the use of LES instead of DNS, unaffordable because of the high Reynolds number, the viscous diffusion 22 and dissipation 23 terms are strongly subject to filtering effects, so it is complex to compute them directly. Also, as the solution is averaged over a large period of time, it can be assumed to be stationary. As a result, the time derivative is assumed to be zero. Moreover, our study focuses on regions far from walls and at high Reynolds numbers. Consequently, viscous diffusion 22 is assumed to be negligible. Following the same methodology as Colombié *et al.* [23], dissipation is therefore deduced from the balance as described in Eq. 28.

$$-\varepsilon_{ij} = C_{ij} - \mathcal{P}_{ij} - \phi_{ij} - \mathcal{D}_{ij}^{t} - \mathcal{D}_{ij}^{p} - \Sigma_{ij} \tag{28}$$

As the objective is to analyse the relative importance of the budget terms, the quantities are scaled by the maximum production of the xx component. So, for example, the xr component of dissipation 23 becomes:

$$\varepsilon^*_{xr} = \frac{\varepsilon_{xr}}{\max\left(\mathcal{P}_{xx}\right)} \tag{29}$$

Two regions were studied. The first zone is at $x = 3D$, close to the nozzle but far enough away from it so as not to be affected by the peak turbulent kinetic energy presents near $x = 2D$. This zone is particularly interesting to analyse the creation of the mixing layer between the jet and the ambient air. The second is at $x = 20D$ to study these terms in the self-similar area.

B. Potential area

The balance of the four non-zero Reynolds stress components is plotted at $x = 3D$ in Fig. 19. The coupling and viscous diffusion terms are negligible and are not plotted to improve the readability of the graph. Dissipation is computed on the assumption of equilibrium described in Eq. 28.

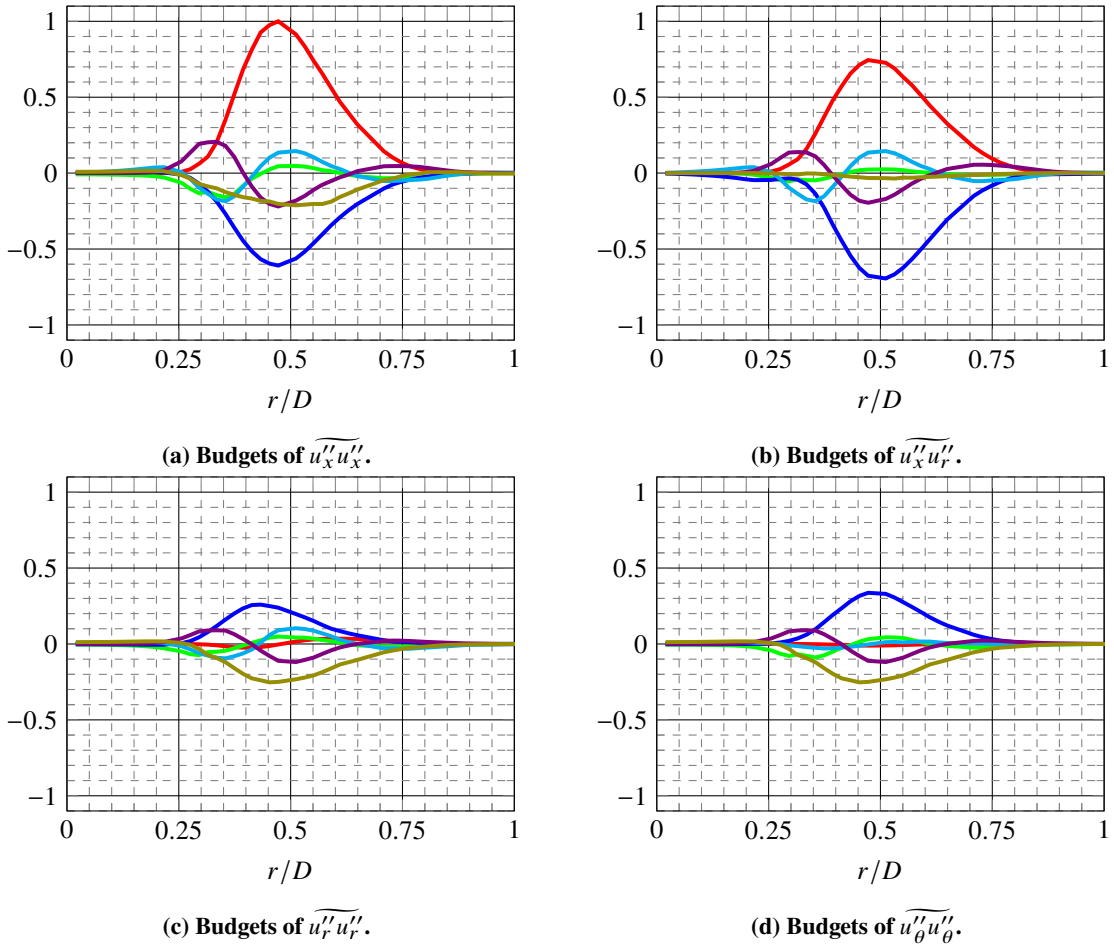

(a) Budgets of $\widetilde{u''_x u''_x}$. **(b) Budgets of $\widetilde{u''_x u''_r}$.**

(c) Budgets of $\widetilde{u''_r u''_r}$. **(d) Budgets of $\widetilde{u''_\theta u''_\theta}$.**

Fig. 19 Radial profiles of the terms making up the Reynolds stress transport equation in the potential area ($x = 3D$): $\mathcal{P}^*_{ij}$, φ^*_{ij}, $-C^*_{ij}$, $\mathcal{D}^{p*}_{ij}$, $\mathcal{D}^{t*}_{ij}$, $-\varepsilon^*_{ij}$.

The balance of the xx and xr components, plotted garphs 19a and 19b respectively, shows several similarities:

1) Production and redistribution terms predominate at $r = D/2$, *i.e.* in the mixing layer created between the jet and the ambient air.
2) Diffusive and convective terms are relatively weak.
3) A balance between production, redistribution and dissipation terms is described in Eq. 30. The turbulence produced by xr et xx components is mostly redistributed to the other components and slightly dissipated in the

xx direction.

$$\mathcal{P}^*_{ij} - \varphi^*_{ij} - \varepsilon^*_{ij} \approx 0 \tag{30}$$

The balance of the rr and $\theta\theta$ components, plotted in Fig. 19c and 19d respectively, initially shows that all terms except dissipation are weaker than those in the xx and xr directions. The present balance between redistribution and dissipation suggests that the turbulence transferred from the xx and xr components to the rr and $\theta\theta$ components of the Reynolds stresses by the redistribution term is directly dissipated by the small scales of the turbulence.

Although the topology of the potential area is strongly impacted by the jet ejection Mach number, similar conclusions can be drawn from the work of Colombié *et al.* [23] and Toutiaei *et al.* [33] on isothermal jets at Mach 0.1 and 0.14 respectively.

C. Self-similar area

The same stress components are plotted in Fig. 20 in the self-similar area at $x = 20D$ as a function of the jet half-opening defined by Eq. 31, and compared with data obtained *via* LES by Bogey *et al.* [22] on an isothermal jet at Mach 0.9. To make the comparison possible, the magnitudes obtained by Bogey are also scaled as described in Eq. 29.

$$U(r = \delta_{0.5}) = \frac{1}{2}U_{axis} \tag{31}$$

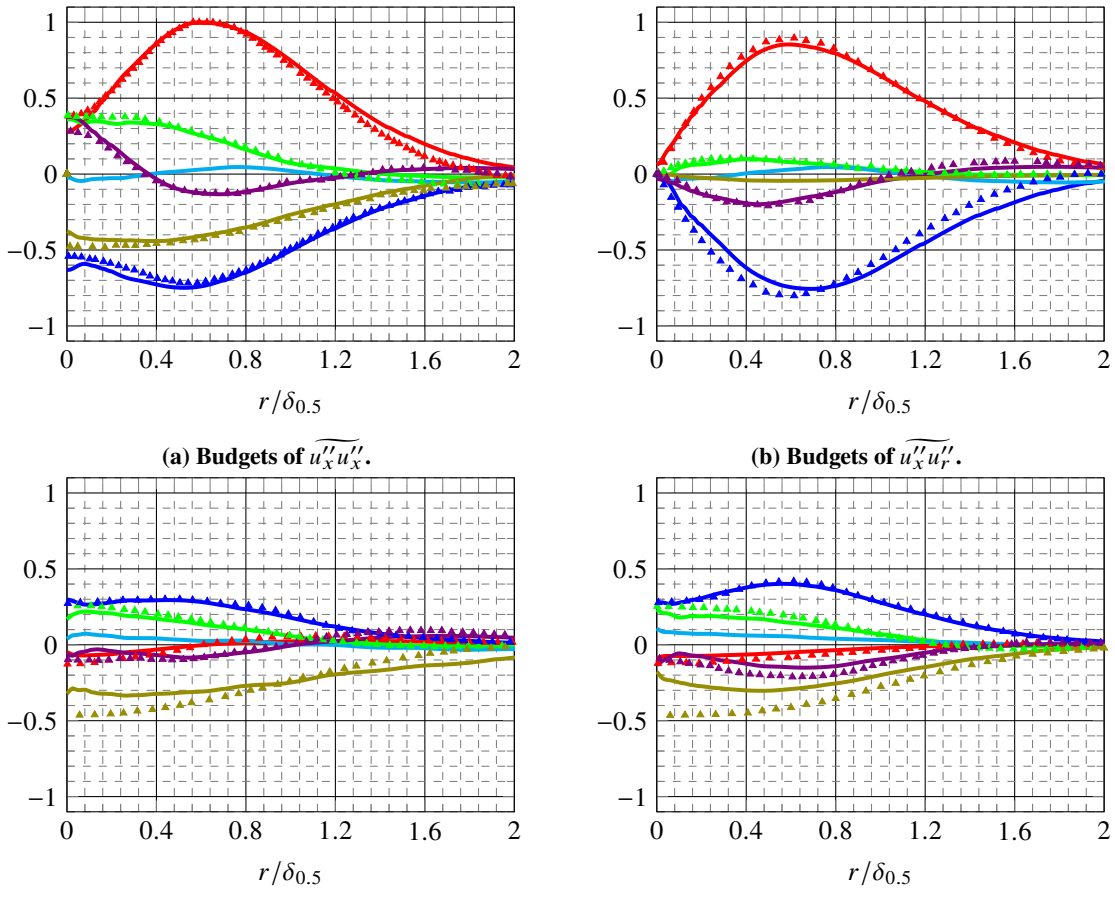

(a) Budgets of $\widetilde{u''_x u''_x}$. **(b) Budgets of $\widetilde{u''_x u''_r}$.**

(c) Budgets of $\widetilde{u''_r u''_r}$. **(d) Budgets of $\widetilde{u''_\theta u''_\theta}$.**

Fig. 20 Radial profiles of the terms making up the Reynolds stress transport equation compute with LES from Bogey [22] (▲) and current study (—) in the self-similar area ($x = 20D$): $\mathcal{P}^*_{ij}$, φ^*_{ij}, $-\mathcal{C}^*_{ij}$, $\mathcal{D}^{p*}_{ij}$, $\mathcal{D}^{t*}_{ij}$, $-\varepsilon^*_{ij}$.

The first observation is that the data obtained from this study is very close to that of Bogey although the Mach difference between the two jets is significant. The results are very different from those obtained in the potential area for the xx component in Fig. 20a. Production still predominates with redistribution, but dissipation, convection and turbulent diffusion become equally important. So, unlike in the potential area, turbulence is partly transferred to the small scales of turbulence and then dissipated, even if an important part is always redistributed.

However, the findings are very close to those found in the potential area for the xr, rr and $\theta\theta$ components. A large part of the turbulence produced by the xr component is redistributed to the other components, and most of it is dissipated by the rr and $\theta\theta$ components.

The relative weight of each term is summarized in table 5. The turbulence cycle shown in Fig. 18 is therefore

Table 5 Predominance of the different terms in the Reynolds stress transport equation.

Area	Direction	$\mathcal{P}^*$	φ^*	$\mathcal{C}^*$	$\mathcal{D}^{t*}$	ε^*
Potential area	xx	++	++	-	-	-
	xr	++	++	-	-	-
	rr	-	++	-	-	++
	$\theta\theta$	-	++	-	-	++
Self similar area	xx	++	++	+	+	+
	xr	++	++	-	-	-
	rr	-	++	-	-	++
	$\theta\theta$	-	++	-	-	++

verified. In the light of the results obtained both close to the nozzle and in the self-similar area, it is clear that the most important terms in the Reynolds stress balance equations are production and redistribution for jet-type flows. Since production is computed and not modelled by RSM, the redistribution term is very important. These results explain Eisfeld's conclusions [30], presented in the introduction, on the importance of calibrating the constants of the redistribution model.

VI. Conclusion

Jets are complex flows to model due to a large number of involved physical phenomena, including a strong turbulence anisotropy. Consequently, the use of RSM-type RANS models seems to be a good choice.

However, the first simulation carried out with the EBRSM model failed to obtain the correct jet behaviour. The aim of this study is therefore to compute the different terms of the Reynolds stress balance to understand which ones are predominant.

First, the LES mean field has been validates on Bridges' experimental data, so the terms making up the Reynolds stress balance could be calculated. A strong predominance of production and redistribution terms is verified, both near the nozzle and in the self-similar area. It is therefore clear that correct modelling of the redistribution term is necessary to obtain accurate results with RANS models containing Reynolds constraints.

Eisfeld's study of the anisotropy rates obtained in a mixing layer with the SSG model suggests that the constants chosen to create this model are not suitable for jets.

In the future, it will be interesting to check whether the constants of the SSG model can be adjusted to improve its reliability for jet flows. In addition, a more in-depth analysis of the dissipation transport equation may also be of interest, given its importance in the Reynolds Stress budgets.

Acknowledgments

This work is supported by ONERA's DAMYSOS research project, which aims to improve the numerical simulation of propulsion jets, and by the MEGeP doctoral school, which is financing B. Desmolin's thesis.

References

[1] "Acoustic loads generated by the propulsion system," NASA-SP-8072, 1971.

[2] Gu, B., Kim, M. Y., and Baek, S. W., "Analysis of the IR Signature and Radiative Base Heating from a Supersonic Solid Rocket Exhaust Plume," *International Journal of Aeronautical and Space Sciences*, Vol. 20, 2019, pp. 423–432. https://doi.org/10.1007/s42405-018-0135-y.

[3] Karnal, M., and Batul, B., "Estimation of exhaust gas temperature of the rocket nozzle using hybrid approach," *Journal of Thermal Science*, Vol. 25, 2016, p. 485–491. https://doi.org/10.1007/s11630-016-0889-0.

[4] Wygnanski, I., and Fiedler, H., "Some measurements in the self-preserving jet," *Journal of Fluid Mechanics*, Vol. 38, No. 3, 1969, pp. 577–612. https://doi.org/10.1017/S0022112069000358.

[5] Hussein, J., Capp, S., and George, W., "Velocity measurements in a high-Reynolds-number, momentum-conserving, axisymmetric, turbulent jet," *Journal of Fluid Mechanics*, Vol. 258, 1994, pp. 31–75. https://doi.org/10.1017/S002211209400323X.

[6] Amielh, M., Djeridane, T., Anselmet, F., and Fulachier, L., "Velocity near-field of variable density turbulent jets," *International Journal of Heat and Mass Transfer*, Vol. 39, No. 10, 1996, pp. 2149–2164. https://doi.org/10.1016/0017-9310(95)00294-4.

[7] Simonich, J., Narayanan, S., Barber, T., and Nishimura, M., "High subsonic jet experiments. I - Aeroacoustic characterization, noise reduction and dimensional scaling effects," *AIAA 2000-2022. 6th Aeroacoustics Conference and Exhibit*, 2002. https://doi.org/10.2514/2.1692.

[8] Narayanan, S., Barber, T., and Polak, D., "High Subsonic Jet Experiments: Turbulence and Noise Generation Studies," *AIAA Journal*, Vol. 40, No. 3, 2002, pp. 430–437. https://doi.org/10.2514/2.1692.

[9] Love, E., Grigsby, C., Lee, L., and Woodling, M., "Experimental and Theoretical Studies of Axisymmetric Free Jets," NASA-TR-R-6, 1959.

[10] Norum, T., and Seiner, J., "Measurements of Mean Static Pressure and Far Field Acoustics of Shock Containing Supersonic Jets," NASA-TM-84521, 1982.

[11] Seiner, J., Ponton, M., Jansen, B., and Lagen, N., "The effects of temperature on supersonic jet noise emission," *DGLR/AIAA 14th Aeroacoustics Conference*, 1992.

[12] Gely, D., Foulon, H., Lambare, H., and Valiere, J., "Overview of aeroacoustic research activities in MARTEL facility applied to jet noise," *Inter-Noise*, 2006.

[13] Wernet, M. P., Georgiadis, N. J., and Locke, R. J., "Velocity, Temperature and Density Measurements in Supersonic Jets," *AIAA 2021-0596. AIAA Scitech 2021 Forum*, 2021. https://doi.org/10.2514/6.2021-0596.

[14] Lau, J., Morris, P., and Fisher, M., "Measurements in subsonic and supersonic free jets using a laser velocimeter," *Journal of Fluid Mechanics*, Vol. 93, 1979, pp. 1–27. https://doi.org/10.1017/S0022112079001750.

[15] Zaman, O., "Asymptotic spreading rate of initially compressible jets, experiment and analysis," *Physics of Fluids*, Vol. 10, No. 10, 1998, pp. 2652–2660. https://doi.org/10.1063/1.869778.

[16] Pope, S. B., *Turbulent Flows*, Cambridge University Press, 2000. https://doi.org/10.1088/0957-0233/12/11/705.

[17] Attili, A., and Bisetti, F., "Statistics and scaling of turbulence in a spatially developing mixing layer at Re= 250," *Physics of Fluids*, Vol. 24, No. 3, 2012, p. 035109. https://doi.org/10.1063/1.3696302.

[18] Oefelein, J. C., "Large-eddy simulation of turbulent combustion processes in propulsion and power systems," *Progress in Aerospace Sciences*, Vol. 42, No. 1, 2006, pp. 2–37. https://doi.org/10.1016/j.paerosci.2006.02.001.

[19] Brès, G., Ham, F., Nichols, J. W., and Lele, S. K., "Nozzle Wall Modeling in Unstructured Large-Eddy Simulations for Hot Supersonic Jet Predictions," *AIAA 2013-2142. 19th AIAA/CEAS Aeroacoustics Conference*, 2013. https://doi.org/10.2514/6.2013-2142.

[20] Fureby, C., "Large-eddy simulation modelling of combustion for propulsion applications," *Philosophical Transactions of the Royal Society A: Mathematical, Physical and Engineering Sciences*, Vol. 367, No. 1899, 2009, pp. 2957–2969. https://doi.org/10.1098/rsta.2008.0271.

[21] Chauvet, N., Deck, S., and Jacquin, L., "Zonal Detached Eddy Simulation of a Controlled Propulsive Jet," *AIAA Journal*, Vol. 45, No. 10, 2007, pp. 2458–2473. https://doi.org/10.2514/1.28562.

[22] Bogey, C., and Bailly, C., "Turbulence and energy budget in a self-preserving round jet: direct evaluation using large-eddy simulation," *Journal of Fluid Mechanics*, Vol. 627, 2009, pp. 129–160. https://doi.org/10.1017/S0022112009005801.

[23] Colombié, A., Laroche, E., Chedevergne, F., Manceau, R., Duchaine, F., and Gicquel, L., "Large-eddy-simulation-based analysis of Reynolds-stress budgets for a round impinging jet," *Physics of Fluids*, Vol. 33, No. 11, 2021. https://doi.org/10.1063/5.0064009.

[24] Pantano, C., and Sarkar, S., "A study of compressibility effects in the high-speed turbulent shear layer using direct simulation," *Journal of Fluid Mechanics*, Vol. 451, 2002, pp. 329–371. https://doi.org/10.1017/S0022112001006978.

[25] Papp, J., and Dash, S., "Turbulence model unification and assessment for high-speed aeropropulsive flows," *AIAA 2001-880. 39th Aerospace Sciences Meeting and Exhibit*, 2001. https://doi.org/10.2514/6.2001-880.

[26] Dash, S., Kenzakowsli, D., Papp, J., Calhoon, W., Arunajatesan, S., Kannepalli, C., and Seiner, J., "Progress in Jet Turbulence Modeling for Aero-Acoustic Applications," *AIAA 2002-2525. 8th AIAA/CEAS Aeroacoustics Conference & Exhibit*, 2002. https://doi.org/10.2514/6.2002-2525.

[27] Ayyalasomayajula, H., Kenzakowski, D., Papp, J., and Dash, S., "Assessment of k-epsilon/EASM Turbulence Model Upgrades for Analyzing High Speed Aeropropulsive Flows," *AIAA 2005-1101. 43rd AIAA Aerospace Sciences Meeting and Exhibit*, 2005. https://doi.org/10.2514/6.2005-1101.

[28] Georgiadis, N., Yoder, D., and Engblom, W., "Evaluation of Modified Two-Equation Turbulence Models for Jet Flow Predictions," *AIAA 2006-490. 44th AIAA Aerospace Sciences Meeting and Exhibit*, 2006. https://doi.org/10.2514/6.2006-490.

[29] Shirzadi, M., Mirzaei, P. A., and Tominaga, Y., "RANS model calibration using stochastic optimization for accuracy improvement of urban airflow CFD modeling," *Journal of Building Engineering*, Vol. 32, 2020. https://doi.org/10.1016/j.jobe.2020.101756.

[30] Eisfeld, B., "Turbulence Modeling for Free Shear Flows," *AIAA 2019-2962. AIAA Aviation 2019 Forum*, 2019. https://doi.org/10.2514/6.2019-2962.

[31] Speziale, C. G., Sarkar, S., and Gatski, T. B., "Modelling the pressure–strain correlation of turbulence: an invariant dynamical systems approach," *Journal of Fluid Mechanics*, Vol. 227, 1991, pp. 245–272. https://doi.org/10.1017/S0022112091000101.

[32] Panchapakesan, N. R., and Lumley, J. L., "Turbulence measurements in axisymmetric jets of air and helium. Part 1. Air jet," *Journal of Fluid Mechanics*, Vol. 246, 1993, pp. 197–223. https://doi.org/10.1017/S0022112093000096.

[33] Toutiaei, S., Semaan, R., and Naughton, J., "Reynolds Stress and Turbulence Kinetic Energy Balances in Swirling Jets," *AIAA 2021-105. 48th AIAA Aerospace Sciences Meeting*, 2010. https://doi.org/10.2514/6.2010-105.

[34] Manceau, R., and Hanjalić, K., "Elliptic blending model: A new near-wall Reynolds-stress turbulence closure," *Physics of Fluids*, Vol. 14, No. 2, 2002, pp. 744–754. https://doi.org/10.1063/1.1432693.

[35] Bridges, J., and Wernet, M. P., "Establishing Consensus Turbulence Statistics for Hot Subsonic Jets," *AIAA 2010-3751. 16th AIAA/CEAS Aeroacoustics Conference*, 2010. https://doi.org/10.2514/6.2010-3751.

[36] NASA, "Turbulence modeling resource," https://turbmodels.larc.nasa.gov/index.html, Consulted on 11/21/2023.

[37] Refloch, A., Courbet, B., Murrone, A., Villedieu, P., Laurent, C., Gilbank, P., Troyes, J., Tessé, L., Chaineray, G., and Dargaud, J., "CEDRE Software," *Aerospace Lab*, Vol. 2, No. 11, 2011.

[38] Guy, A., Fromentin-Denoziere, B., Phan, H.-K., Cheraly, A., Gueyffier, D., Rialland, V., Erades, C., Elias, P., Labaune, J., Ristori, A., Brossard, C., and Rommeluere, S., "Ionized solid propellant rocket exhaust plume: MiLES simulation and comparison to experiment," *7th European Conference for Aeronautics and Space Sciences*, Vol. 25, 2017, pp. 1–19. https://doi.org/DOI:10.13009/EUCASS2017-434.

[39] Gueyffier, D., Fromentin-Denoziere, B., Simon, J., Merlen, A., and Giovangigli, V., "Numerical simulation of ionized rocket plumes," *Journal of Thermophysics and Heat Transfer*, Vol. 28, 2014, pp. 218–225. https://doi.org/10.2514/1.T4239.

[40] Langenais, A., Vuillot, F., Troyes, J., and Bailly, C., "Accurate simulation of the noise generated by a hot supersonic jet including turbulence tripping and nonlinear acoustic propagation," *Physics of Fluids*, 2019, 31 (1): 016105. https://doi.org/10.1063/1.5050905.

[41] Alomar, A., Nicole, A., and Sipp, D., "Reduced-order model of a reacting, turbulent supersonic jet based on proper orthogonal decomposition," *Theoretical and Computational Fluid Dynamics*, Vol. 34, 2020, pp. 49–77. https://doi.org/10.1007/s00162-019-00513-y.

[42] Scherrer, D., Chedevergne, F., Grenard, P., Troyes, J., and Murrone, A., "Recent CEDRE Applications," *Aerospace Lab*, Vol. 2, No. 13, 2011.

[43] Mitchell, C., and Walters, R., "K-exact reconstruction for the Navier-Stokes equations on arbitrary grids," *AIAA 1993-536. 31st Aerospace Sciences Meeting*, 1993. https://doi.org/10.2514/6.1993-536.

[44] Harten, A., Lax, P., and van Leer, B., "On upstream differencing and Godunov-type schemes for hyperbolic conservation laws," *44th AIAA Aerospace Sciences Meeting and Exhibit*, Vol. 25, No. 1, 1983, pp. 35–61. https://doi.org/10.1137/1025002.

[45] Courbet, B., Benoit, C., Couaillier, V., Haider, F., Le Pape, M. C., and Péron, S., "Space Discretization Methods," *Aerospace Lab*, Vol. 2, No. 6, 2011.

[46] Favre, A., "De la causalité à la finalité: à propos de la turbulence," *Collection Recherches interdisciplinaires*, Vol. 30, 1988.

[47] Manceau, R., "Recent progress in the development of the Elliptic Blending Reynolds-stress model," *International Journal of Heat and Fluid Flow*, Vol. 51, 2015, pp. 195–220. https://doi.org/10.1016/j.ijheatfluidflow.2014.09.002.

[48] Vreman, A. W., Geurts, B. J., and Kuerten, J. G. M., "Large-eddy simulation of the turbulent mixing layer," *Journal of Fluid Mechanics*, Vol. 339, 1997, pp. 357–390. https://doi.org/10.1017/S0022112097005429.

[49] Smagorinsky, J., "General Circulation Experiments with the Primitive Equations: I. The basic Experiment," *Monthly Weather Review*, Vol. 91, 1993, p. 99–164. https://doi.org/10.1175/1520-0493(1963)091<0099:GCEWTP>2.3.CO;2.

[50] Menter, F., "Two-equation eddy-viscosity turbulence models for engineering applications," *AIAA Journal*, Vol. 32, 1994, pp. 1598–1605. https://doi.org/10.2514/3.12149.

[51] Antares Development Team, "Antares Documentation Release 2.1.0," https://cerfacs.fr/antares/, Consulted on 04/13/2023.

[52] Bogey, C., Marsden, O., and Bailly, C., "Influence of initial turbulence level on the flow and sound fields of a subsonic jet at a diameter-based Reynolds number of 10^5," *Journal of Fluid Mechanics*, Vol. 701, 2012, p. 352. https://doi.org/10.1017/jfm.2012.162.

[53] Lorteau, M., Cléro, F., and Vuillot, F., "Analysis of noise radiation mechanisms in hot subsonic jet from a validated large eddy simulation solution," *Physics of Fluids*, Vol. 27, No. 7, 2015. https://doi.org/10.1063/1.4926792.

[54] Delville, J., Bellin, S., Garem, J., and Bonnet, J., "Analysis of Structures in a Turbulent, Plane Mixing Layer by Use of a Pseudo Flow Visualization Method Based on Hot-Wire Anemometry," *Advances in Turbulence 2*, 1989, pp. 251–256. https://doi.org/10.1007/978-3-642-83822-4_38.

[55] Leschziner, M., *Statistical Turbulence Modelling for Fluid Dynamics — Demystified*, Non-Series Books, 2015. https://doi.org/10.1142/p997.